Chemical Engineering Journal 450 (2022) 138412

Contents lists available at ScienceDirect

Chemical Engineering Journal

journal homepage: www.elsevier.com/locate/cej

Scaled-up multistage reverse electrodialysis pilot study with natural waters

Catarina Simões [a,b,*], Bárbara Vital [a,c], Tom Sleutels [a,d], Michel Saakes [a], Wim Brilman [b]

[a] Wetsus, European Centre of Excellence for Sustainable Water Technology, P.O. Box 1113, 8900 CC Leeuwarden, the Netherlands
[b] Sustainable Process Technology, Faculty of Science and Technology, University of Twente, P.O. Box 217, 7500 AE Enschede, the Netherlands
[c] Environmental Technology, Wageningen University and Research, P.O. Box 17, 6700 AA Wageningen, the Netherlands
[d] Faculty of Science and Engineering, University of Groningen, Nijenborgh 4, 9747 AG Groningen, the Netherlands

ARTICLE INFO

Keywords:
Renewable energy
Pilot testing
Multistage reverse electrodialysis
Natural waters
Salinity gradient power

ABSTRACT

A multistage reverse electrodialysis system was studied at the REDstack research facility (the Afsluitdijk, the Netherlands) for over 30 days to describe the performance of such configuration under natural water conditions. The experiments were done with two 0.22 × 0.22 m^2 stacks in series comprising 32 cell pairs (3.1 m^2 of membrane area) for stage 1 and 64 cell pairs (6.2 m^2 membrane area) for stage 2. The total gross power density at the available salinity gradient was stable at around 0.35 $W \bullet m^{-2}$. The total net power density, corrected for the initial pressure drop of the stacks, was 0.25 $W \bullet m^{-2}$ at an energy efficiency of 37 %. Throughout the operation, due to increased stack pressure drop, the actual total net power density lowered to 0.1 $W \bullet m^{-2}$. A distinct behaviour was found for multivalent ions in each stage. For stage 1, Ca^{2+} and SO_4^{2-} were transported from the river water to the seawater side, so-called uphill transport. For stage 2, uphill transport was not found, in line with Donnan potential calculations. Stack autopsy revealed microorganisms with sizes ten times larger than the cartridge filter nominal pore size (5 μm) and biofilm covering part of the spacer open area, both contributing to the increasing pressure drop in the stacks. This study showed that stable gross power densities and high energy efficiencies were obtained from feeding natural waters to a multistage reverse electrodialysis system, independent of fouling. In addition, it emphasized the importance of maintaining pumping power losses low for a viable deployment of the technology.

1. Introduction

Renewable energy sources are a key element in fighting climate change, and CO_2 emissions and, simultaneously help fulfilling world energy requirements. One renewable energy source is salinity gradient energy (SGE), also known as "Blue Energy". SGE results from the chemical potential difference between two solutions of different salinity, for instance, while mixing seawater and river water [1].

Reverse electrodialysis (RED) is an electro-membrane process that harvests the SGE in the form of electrical energy, using cation and anion exchange membranes (CEMs and AEMs) alternately piled in a stack [2]. Spacers keep the membranes apart and make the compartments to flow the feed solutions. Seawater and river water are fed alternately through these compartments. During operation, the concentration gradient across the membranes leads to ion transport from the seawater to the river water compartment and according to their selectivity, CEMs transport cations and AEMs transport anions. The resulting ionic current, generated through the stack, is converted into electric current, usually through redox reactions at the electrode end compartments [3].

The RED process was already introduced in 1954 [4]. However, it only gained more attention in the last two decades due to the call for new renewable energy sources and advances in ion-exchange membranes' performance and fabrication [5]. Despite technological advances during the last decade [6,7], the process has not yet met the targeted power density output of 2 $W \cdot m^{-2}$ and energy efficiency of 40 % at long-term operation [8]. This is particularly true when natural waters are used, demonstrating the need to study natural water systems for the end application. Experiments towards natural seawater and river water applications have investigated the presence of divalent ions (e.g. Ca^{2+}, Mg^{2+}, SO_4^{2-}) which resulted in a decrease in the gross power density compared to NaCl solutions [9–12]. This is due to uphill transport, where divalent ions are exchanged with monovalent ions and are transported against the direction of the concentration gradient, and due to the larger hydration radius of divalent ions which increases the membrane electrical resistance. The use of monovalent selective ion exchange membranes has shown improvements in the gross power

* Corresponding Author at: Wetsus, European Centre of Excellence for Sustainable Water Technology, P.O. Box 1113, 8900 CC Leeuwarden, the Netherlands.
E-mail address: catarina.simoes@wetsus.nl (C. Simões).

https://doi.org/10.1016/j.cej.2022.138412
Received 22 April 2022; Received in revised form 22 July 2022; Accepted 29 July 2022
Available online 1 August 2022

density [13–15]. Changes in temperatures have also been assessed, showing that lower temperatures affect negatively the performance of RED [16,17]. Other studies, focused on the fouling in natural waters, indicate that, when no anti-fouling strategies are in place, organic matter can decrease the gross power density up to 40 %, whereas inorganic fouling can decrease up to 8 % [18,19]. anti-fouling strategies, such as water pre-treatment [20], cleaning strategies [21,22] or RED monitors [23,24] show a prospect of solving fouling issues and maintaining low stack pressure drops with the challenge of using less energy. The use of profiled membranes [25,26] was also suggested to decrease stack pressure drops. Another challenge brought by natural waters is the possible scaling at the electrodes of, for example, $Mg(OH)_2$ and $CaCO_3$, which increased the energetic losses [27]. However, studies combining natural seawater and river water with control strategies, such as electrode segmentation [28] and multistage [29], are missing in the literature.

Multistage RED (MSRED) concept is gaining more attention as it increases the power output, consequently, the energy efficiency, while keeping the gross power density higher when compared to a single stage in the same conditions. MSRED enables different currents per electrode pair, as in electrode segmentation [28]. Moreover, it allows different configurations and materials per stage which can further improve the performance [30]. Veerman, who was the first to propose the MSRED concept in 2009 [31], recently published a model-based study with co– and counter-current flow in different multistage arrangements for maximum efficiency with different electrical controls [32]. Tedesco et al. simulated cross-flow stacks for brine and brackish water mixtures up to three stages and 500 cell pairs per stage, showing more than 1000 W could be obtained [33]. Hu et al. showed through modelling that a multistage series control was more suitable in practice with a counter-flow arrangement for brine and river water concentrations in a RED heat engine system [29]. Their work continued with an experimental investigation where the process efficiency was five times higher than with single-stage, preferably using low feed flow velocities [34]. Referring to natural waters, Wang et al. studied MSRED with natural seawater and brine to improve the process energy efficiency. However, the water composition was left out (only overall concentration was given), the test duration was rather short and only one stack was used to simulate the staging effect [35]. Besides the energy production aspect, MSRED is also used for improving the decolourization efficiency of azo dye wastewater [36], creating a system combined with multi-effect distillation [37] or producing hydrogen [38].

Our previous work investigated the application of MSRED for seawater and river water through modelling and experiments, using 0.5 M and 0.017 M NaCl solutions [30]. We concluded that the total power density and energy efficiency increased with a two-stage configuration using the "saving the gradient" strategy (stage 1 operated at a current density below the stage maximum power density) to achieve an overall higher maximum power. In addition, the pressure drop inherent to the feed compartments played an important role in the staging implementation [30]. Later on, the same multistage model was extended to include magnesium and sulphate ions in solution but it was validated only with single-stage experiments in controlled conditions [39]. The advantages of MSRED were moderated with the presence of divalent ions. The behaviour of multivalent ions in MSRED is limited to the model study and not experimentally verified. Thus, long-term testing of MSRED with natural seawater and river water, connecting two cross-flow stacks in series, where the multivalent ions impact and fouling are evaluated daily, to our knowledge, has never been reported before.

In this study, we show for the first time the performance of two 0.22 × 0.22 m^2 cross-flow stacks connected in series, fed with natural seawater and river water, at a geographical relevant location for RED implementation, over more than 30 days. The goal was to understand the impact of natural waters in an MSRED system concerning performance, ion transport and fouling and dealing with fluctuations associated with nature. Initially, the stacks were individually characterized at the laboratory using pure NaCl solutions (30 and 1 g $NaCl \bullet L^{-1}$) and, later were transported to the REDstack research facility (Afsluitdijk, the Netherlands), which allowed continuous water supply, and connected in series. During 30 days, the MSRED fed with natural waters was monitored continuously, revealing the fate of the ions (in particular divalent ions) and process performance. After a month of operation, cleaning techniques were tested in an attempt to lower the pressure drop across the stacks. At the end of the operation, a stack autopsy was conducted to evaluate the fouling extension.

2. Materials and methods

2.1. Experimental setups

Two cross-flow RED stacks were provided and built by REDstack BV (Sneek, the Netherlands). The details of the stack design can be found elsewhere in the literature [40]. The stacks were connected in series with the river and seawater both fed to stack 1 and stack 2 received the outlet streams of stack 1 (Fig. 1). Stack 1 (or stage 1), which was the first stack receiving the feed waters in the multistage configuration, contained 32 cell pairs (3.098 m^2 of total active membrane area) and stack 2 (or stage 2) contained 64 cell pairs (6.196 m^2 of total active membrane area). The difference in the number of cell pairs resulted from model simulations, a shorter residence time increases the power density on stage 1 and a longer residence time, on stage 2, will exhaust further the salinity gradient increasing the energy efficiency while having lower pumping losses [30]. The active area of a single membrane was 0.22 m × 0.22 m. Each cell pair comprised one CEM (Fumasep FKS-30, Fumatech GmbH, Germany) and one AEM (Fumasep FAS-30, Fumatech GmbH, Germany). The shielding membranes were two fluorinated CEMs (Fumatech F-10150-PTFE, Fumatech GmbH, Germany), one being part of a cell pair and the other as the extra membrane. The ion exchange membranes properties can be seen in Table 1. Woven net spacers of 155 μm thickness (Deukum, GmbH, Germany) were used to make the compartments, with 55 % porosity. At the endplates, a pair of 0.22 m × 0.22 m platinized Ti-mesh electrodes were used as anode and cathode (MAGNETO special anodes BV, the Netherlands).

The experiments were conducted first at the laboratory at Wetsus, for stacks validation with NaCl solutions, and later at the REDstack BV research facility (the Afsluitdijk, the Netherlands), where it took place the transition to natural feed waters and set up for two section 3.1), the 30-day run experiment (section 3.2 and 3.3) and only after the cleaning strategies and fouling investigation (section 3.4).

The electrode rinse solution (ERS), during the laboratory tests and first days of the pilot tests, was a mixture of 0.2 M $K_4Fe(CN)_6$, 0.2 M $K_3Fe(CN)_6$ and 0.15 M NaCl (VWR Chemicals, Belgium) recirculated at 300 $mL \bullet min^{-1}$. Although it worked in the laboratory and also with natural feed waters at a smaller scale [42,43], the hexacyanoferrate solution was found not to be suitable for scaled-up stacks using natural feed waters. Mg^{2+} and Ca^{2+} ions crossed the CEMs and reacted with OH^- resulting from the reduction of water at the cathode and precipitated as salts. Figure S1 shows the visual difference between the initial pristine solution and the used ERS in each stage and, Figure S2 shows the scaling found at the autopsy. Therefore, to avoid scaling at the cathode, the ERS was replaced with single-pass seawater. Each electrode compartment for each stage was fed with seawater independently at a rate of 600 $mL \bullet min^{-1}$. Ag/AgCl reference electrodes were used to measure the potential difference across the membrane pile, excluding the overpotential at the electrodes. In a commercial application, voltages losses due to oxygen, chlorine and hydrogen evolution reactions need to be taken into account (around 1.5 to 2 V) or ERS that avoid such loss should be developed.

The laboratory setup has been described in our previous work [30]. For the pilot setup (Fig. 1), the river water (RW) and seawater (SW) were pumped at a flow rate of 39.3 $L \bullet h^{-1}$, corresponding to 1.0 $cm \bullet s^{-1}$ in stage 1 and 0.5 $cm \bullet s^{-1}$ in stage 2, unless stated another flow rate. The

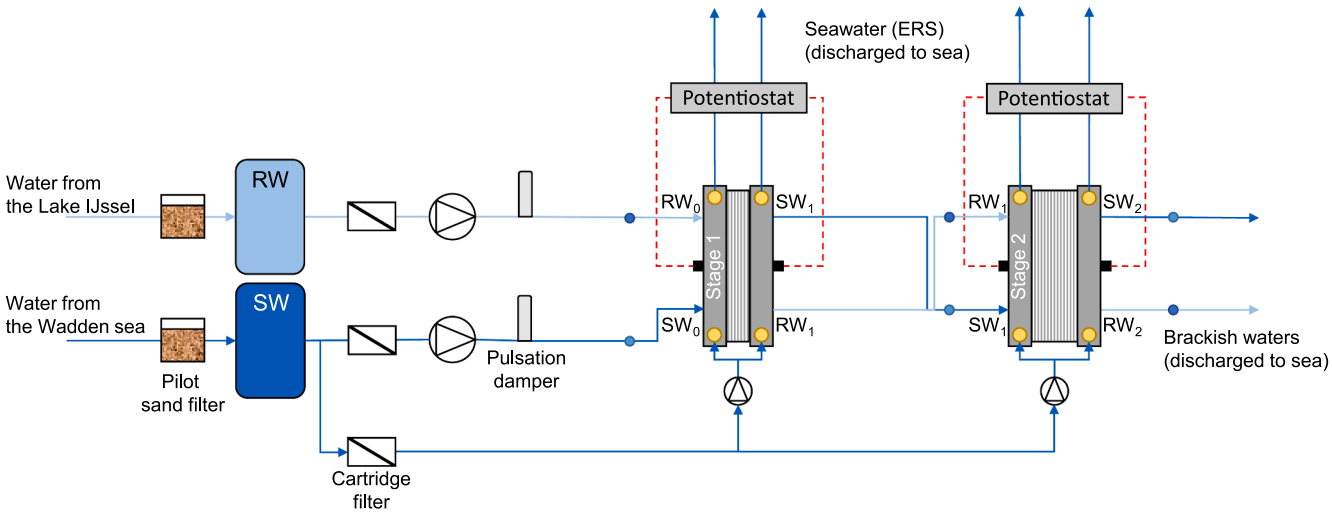

Fig. 1. Schematic diagram of the experimental setup at the research facility fed with river water (RW) and seawater (SW) and with single-pass seawater as the electrode rinse solution. Dots represent the sampling points in positions 0, 1 and 2. The three-way valves for water switching are not represented for simplicity but were installed before the stage 1 inlet.

Table 1
Ion exchange membranes properties.

Properties	FKS-30	FAS-30	F-10150-PTFE
Thickness (dry) [α] [μm]	25–35	25–35	140 – 150
Permselectivity [α] [%]	>98	>90	>95
Electrical resistance [β] [Ω·cm^2]	1.32	0.78	1.8 – 2.9 [γ]
Ion exchange capacity [γ] [meq·g^{-1}]	1.43	1.6 – 2.0	0.7 – 0.9
Dimensional swelling in H2O [α] [%]	< 3	< 2	< 5

[α] Fumatech Technical Data Sheet, provided upon the membrane purchase.
[β] Measured in a six-compartment cell at 0.5 M NaCl, according to a literature procedure[41].
[γ] FUELCELL Store Technical Data Sheet, available online (www.fuelcellstore.com/fumatech).

spacer porosity was not included in the flow velocity calculation. The natural feed waters were automatically switched (changing compartment) every-six hours to further mitigate scaling at the electrode compartments. By switching the feed waters, thus the polarity of the stack, cathode and anode were switched periodically, which helped lowering inorganic scaling at the cathode. Both valves installed for water switching were controlled by a Raspberry Pi (Raspberry Pi Foundation, United Kingdom), using an open-source Python code. Temperature and conductivity (Type 8228, Burkert, Germany) were measured inline, before stage 1 (position 0), between stages 1 and 2 (position 1) and after stage 2 (position 2). The pressure drop between inflow and outflow over the stack was measured with absolute pressure sensors (MIDAS SW, JUMO GmbH, Germany). Data were collected with a data logger (Yokogawa, Japan).

At the laboratory, both stacks were fed with pure NaCl solutions (Regenit, Esco, the Netherlands), which consisted of 1 g•L^{-1} for the RW and 30 g•L^{-1} for the SW at 24.5 ± 0.5 °C. These values were chosen for consistency with previous studies with pure NaCl solutions. Afterwards, at the REDstack BV research facility at the Afsluitdijk, the Netherlands, the stacks were fed with natural waters from Lake IJssel (RW) and the Wadden Sea (SW), after being pre-treated with the research facility drum and sand filters, which was the pre-treatment adopted for this study, and a 50 μm/5 μm nominal cartridge filter (Pentek DGD-5005–20, Pentair, USA) placed before the pumps. These waters were sampled at positions 0, 1 and 2 from both RW and SW (Fig. 1), and were characterized with an Ion Chromatograph (Metrohm Compact IC Flex 930, the Netherlands) for Cl^-, SO_4^{2-}, Na^+, K^+, Mg^{2+} and Ca^{2+}. Before analysis, the samples were filtered using a 0.45 μm filter (Merck Millipore Millex-LCR, Germany). The typical composition of the natural feed waters, during the experiment, is given in Table 2.

2.2. Electrochemical measurements and calculations

The electrochemical measurements were done with a two-channel potentiostat (IVIUM *n*-stat, IVIUM Technologies BV, the Netherlands) and recorded with the IVIUMsoft software. The potential across the membrane, in volts, was calculated through the Nernst equation:

$$E = \frac{RT}{zF} ln\left(\frac{m_{SW} \bullet \gamma_{\pm,SW}}{m_{RW} \bullet \gamma_{\pm,RW}}\right) \quad (1)$$

Where R is the gas constant (J.mol^{-1}.K^{-1}), T is the absolute temperature (K), z is the ion valency (−), F is the Faraday constant (C.mol^{-1}), m is the molality (mol•kg H_2O^{-1}) and $\gamma_\pm$ is the mean salt activity coefficient (−) estimated with the model of Ge et al. [44]. For the case of calculating the theoretical open circuit voltage (OCV) Eq. (1) was adapted to $OCV = E \bullet 2N \bullet \alpha_{IEM}$, where N is the number of cell pairs (−) and α_{IEM} is the average of the AEM and CEM permselectivity (−). The experimental OCV was measured when there was no current applied.

To define the power curve and maximum power density an I-V (current–voltage) measurement was done. It consisted of current steps of −0.5 A (at the Wetsus laboratory), and −0.4 A for stage 1 and −0.2 A for stage 2 (with natural waters at the Afsluitdijk) until the cell voltage reached zero. Displaying the results both current and voltage are made positive. The gross power density ($P_{d,gross}$ in W•m^{-2}) of each stage was:

$$P_{d,gross} = \frac{I \bullet U}{A_{mem}} \quad (2)$$

Where I is the current applied (A), U is the measured potential (volts) and A_{mem} is the total active membrane area (m^2). The net power density (Eq. (S1)) only considered pressure drop losses from the stack (Eq. (S2)). For the total power density ($P_{d,total}$ in W•m^{-2}) of two stages, the contribution of each stage needs to be considered:

$$P_{d,total} = \frac{N_{S1}}{N_T} P_{dS1} + \frac{N_{S2}}{N_T} P_{dS2} \quad (3)$$

Where N_T is the total amount of cell pairs (−) and N_{S1} is the amount of cell pairs in stage 1 and N_{S2} is the amount of cell pairs in stage 2. To evaluate the power density and energy efficiency in the long term, the current was fixed during the experiments, after manually employing the

Table 2
Average natural seawater (SW) and river water (RW) characteristics during the experiment at the Afsluitdijk research facility.

Source	Conductivity [mS•cm^{-1}]	Temperature [°C]	Typical ion concentration [mM] Cl^-	SO_4^{2-}	Na^+	K^+	Mg^{2+}	Ca^{2+}
Wadden Sea (SW)	31.4	18.6	342.5	17.9	283.8	6.2	33.2	6.8
	±4.1	±0.6	±37.6	±1.8	±32.6	±0.8	±3.8	±0.7
Lake IJssel (RW)	0.52	19.0	2.7	0.6	2.3	0.1	0.5	1.1
	±0.02	±0.7	±0.2	±0.1	±0.2	±0.1	±0.1	±0.1

"saving the gradient" strategy for the first days [30]. The strategy consisted of stage 1 working at 80 % of its maximum power density and stage 2 at 95 %. Providing a lower current to stage 1 to allow an "extra" salinity gradient for the following stage has proven that more power can be harvested than by setting each stage sequentially at its maximum power [30]. Applied current values and measured response voltage during the 30-day run are shown in Table S1.

To verify how much of the available salinity gradient energy was harvested, the energy efficiency was calculated:

$$\eta = \frac{P_{gross}}{\Delta G_{in}} \tag{4}$$

Where the P_{gross} is the total gross power (W) and the ΔG_{in} is the Gibbs free energy per second at the inlet (W) [45]. To calculate ΔG, the entropy (ΔS in W•K^{-1}) and the absolute temperature (T in K) are needed.

$$\Delta G = \Delta S \bullet T \tag{5}$$

$$\Delta S = S_{mix} - S_{RW} - S_{SW} \tag{6}$$

$$S = -R \bullet n_T \bullet \sum_i x_i ln x_i \bullet \gamma_i$$

$$i = H_2O, Cl^-, Na^+, K^+, SO_4^{2-}, Mg^{2+}, Ca^{2+} \tag{7}$$

Where n_T is the total number of moles (mol.s^{-1}), x_i is the mole fraction (−) and γ_i corresponds to the single ion activity coefficient of species i (−) as specified above. The single ion activity coefficient of species i, γ_i, was approximated by the mean salt activity coefficient, $\gamma_{\pm}$, for the following ions: $\gamma_{Cl^-} = \gamma_{NaCl}$, $\gamma_{Na^+} = \gamma_{NaCl}$, $\gamma_{K^+} = \gamma_{KCl}$, $\gamma_{SO_4^{2-}} = \gamma_{Na_2SO_4}$, $\gamma_{Mg^{2+}} = \gamma_{MgCl_2}$ and $\gamma_{Ca^{2+}} = \gamma_{CaCl_2}$. γ_{H_2O} was assumed 1. With Eqs. (5)–(7), the available power for mixing is calculated.

2.3. Cleaning and autopsy techniques

Cleaning strategies were implemented after more than 30 days of experiment, in an attempt to mitigate the reduction in net power density output. Both stages had visible signs of fouling and presented an increasing pressure drop with time. In the cleaning procedure, the inlet and outlet of the stacks were reversed, since most particulate fouling accumulated in the entrance of the stack and, by reversing the flow direction, this accumulation was pushed out of the stack. Following, the flow was doubled for 5 min, forcing the particles out. After that, air sparging was performed, with a configuration of 3 pulses of 2 s duration each at 3 bar air pressure. Air sparging is a sudden disturbance on the membrane and spacers surface by introducing compressed air for a short time along with the feedwater flow, to remove a large accumulation of foulants, mostly particulate fouling. During the cleaning procedure, water samples were taken at the outlet of each stack compartment (both river and seawater) and were analysed for suspended solids, according to the Standard Methods for the Examination of Water and Wastewater [46].

The multistage configuration was let to run for two more weeks after the cleaning, and at the end of the experiment, stack 1 was carefully opened and investigated concerning fouling. Since a membrane autopsy was destructive to the stack, stack 2 was kept intact for future research. Pictures of the AEM, CEM, spacers and electrodes were taken and membrane and spacer pieces were cut for optical and electron microscopic investigation, always on an inlet, central area of the membrane. The procedure was the same as described in Vital et al. [20]. In short, membrane and spacer pieces were fixed and dried for microscopy analyses under scanning electron microscopy (SEM) and energy-dispersive X-ray spectroscopy (EDX), while other pieces were stained with Alcian Blue 8 GX 0.1 % solution (Sigma Aldrich, the Netherlands) and observed with phase-contrast microscopy (Olympus BX40, Japan) at 10x and 20x magnification, for visualization of organic fraction of extracellular polymeric substances (EPS) and biofilm [47].

3. Results and discussion

3.1. Transitioning between artificial and natural conditions

Both RED stacks were first tested at the laboratory, using pure NaCl solutions and at the same flow velocity (1.0 cm•s^{-1}) to ensure reproducibility. Inlet conditions are shown in Table 3. OCV values were, 0.131 V and 0.133 V per cell pair for stacks 1 and 2, respectively (Fig. 2A). These values are close to the calculated theoretical OCV of 0.150 V per cell pair (Eq. (1), assuming permselectivity, α = 0.95). The power density versus current density curves were similar (Fig. 2B). Stack 1 had a 1.5 % higher gross power density; this minor difference can be attributed to different factors together, such as manual building or ionic shortcut currents from the increased cell pair number in stack 2 [48,49].

When the testing under natural conditions (Fig. 2C and 2D), the stacks were connected in series (Fig. 1), and are now referred to as stages 1 and 2. The initial test conditions can be seen in Table 3. As a consequence of staging, the salinity gradient available for stage 2 is lower than stage 1, due to the mixing in stage 1. Furthermore, since stage 2 has twice the amount of cell pairs of stage 1, the flow velocity is halved to 0.5 cm•s^{-1}. These two factors account for the 2.3 times lower maximum power density in stage 2, shown in Fig. 2D. The effect of staging combined with the change in flow velocity seen here is comparable to the literature for NaCl solutions [30]. The maximum gross power density achieved in stack 1 lab was reduced by 41 % with stage 1 NW (Fig. 2B and 2D). This was due to a combination of effects including the lower salinity gradient available which can be seen in Table 3 and calculated through Eq. (5), and the presence of multivalent ions like Mg^{2+} and Ca^{2+} (details in section 3.3). Vermaas et al. (2014) also reported a decrease of around 50 % in gross power density with $MgSO_4$ (10 %)/ NaCl (90 %) solutions with a total salt concentration of 0.508 M and 0.017 M in artificial seawater and river water [10]. The lower temperature (Table 3), known to negatively influence the power density [11,17], further reduced the gross power density. The maximum gross power density of stage 2 NW (Fig. 2B and 2D) was even lower (0.30 W·m^{-2}) because of the reasons mentioned above concerning initial concentration and flow velocity. Transitioning to natural waters shows multiple challenges that cannot be studied simultaneously in the laboratory.

3.2. Continuous staging performance over a month

Fig. 3 shows the gross power density and energy efficiency on the sampling moments for each stage and in total. Throughout the 30-day run, the total gross power density was quite stable at around 0.35 W•m^{-2} (Eq. (3)). The contribution of each stage can be seen in Fig. 3A,

Table 3
Test description and conditions for each stack/stage. At the laboratory reproducibility tests took place, thus the stacks are studied individually under equal conditions. At the research facility, the stacks, now named stages are already investigated in the two-stage series configuration.

Test	Inlet conditions	SW		RW		Composition	Flow velocity
		σ [mS·cm^{-1}]	T [°C]	σ [mS·cm^{-1}]	T [°C]		[cm.s^{-1}]
Validation	Stack 1 Lab	47.83	24.9	2.03	24.8	NaCl	1.0
Reproducibility	Stack 2 Lab	47.78	25.3	2.03	25.1	NaCl	1.0
Natural conditions	Stage 1 NW	35.33	19.4	0.66	19.5	Natural	1.0
	Stage 2 NW	29.85	19.7	4.60	19.5	Natural	0.5

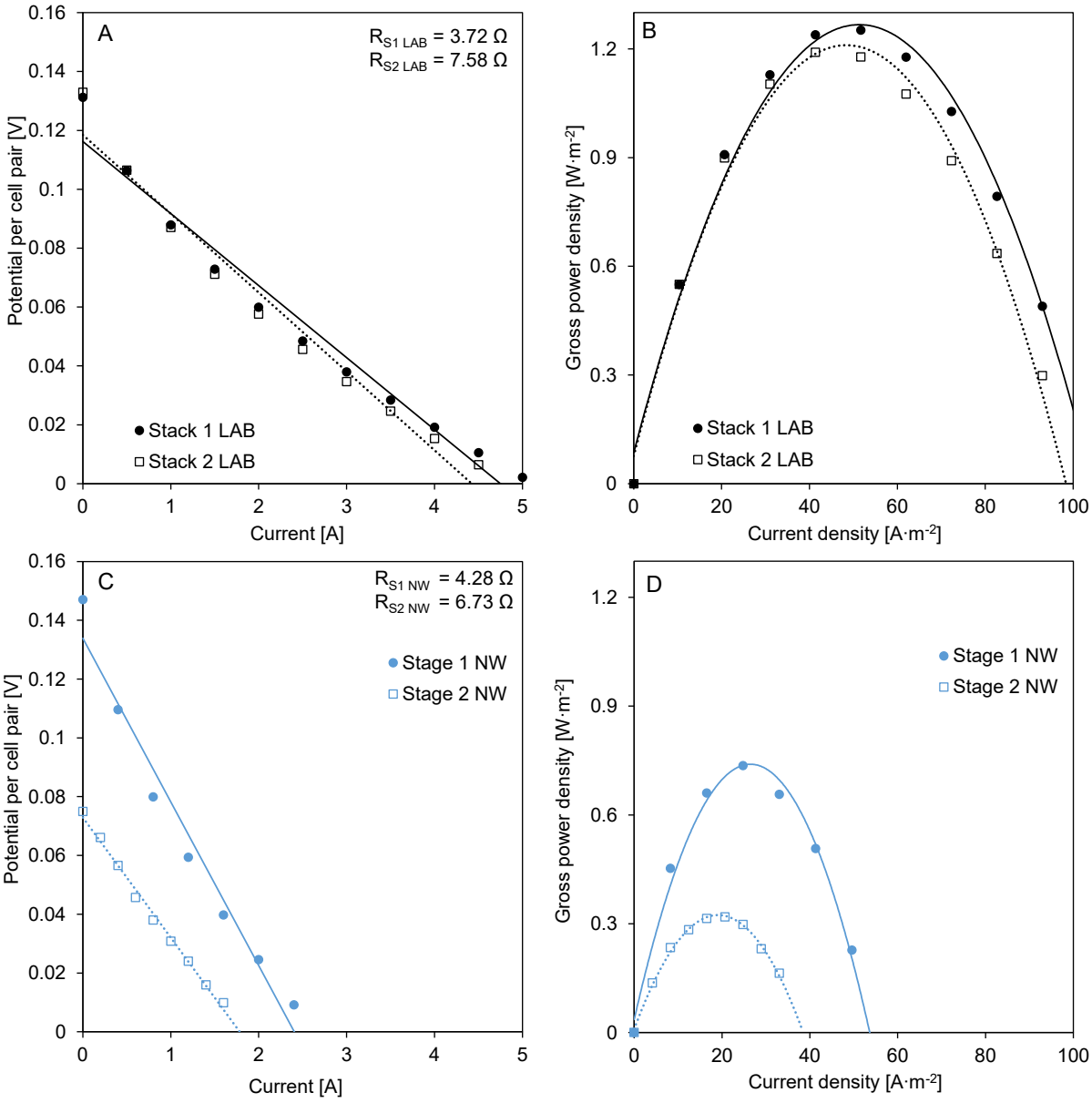

Fig. 2. (A) I-V curve, stack resistance and (B) gross power density vs current density for stacks 1 (circles and solid lines) and 2 (squares and dotted lines) as tested in the laboratory (LAB, black); (C) I-V curve, stack resistance and (D) gross power density vs current density for stages 1 (circles and solid lines) and 2 (squares and dotted lines) as tested at the research facility with natural waters (NW, blue). Conditions for these results are shown in Table 3. In these measurements ERS was still 0.2 M $K_4Fe(CN)_6$, 0.2 M $K_3Fe(CN)6$ and 0.15 M NaCl. Trend lines are added to guide the eye.

averaging 0.55 W•m^{-2} for stage 1 and 0.25 W•m^{-2} for stage 2 (Eq. (2)). By reusing the waters in stage 2, thus extending their use at a reduced salinity gradient, and because of the longer residence time in this stage, there was an expected decrease in total power density. The energy efficiency achieved values above 30 % with a maximum of 37 % (Fig. 3B, Eq. (4)). Such energy efficiencies have not been reported for natural water studies, and are found here to be comparable to theoretical [39,50] and laboratory studies [30,42]. The gross power density and the gross energy efficiency represent a good electrical performance of the multistage configuration. The gross power density would be increased if

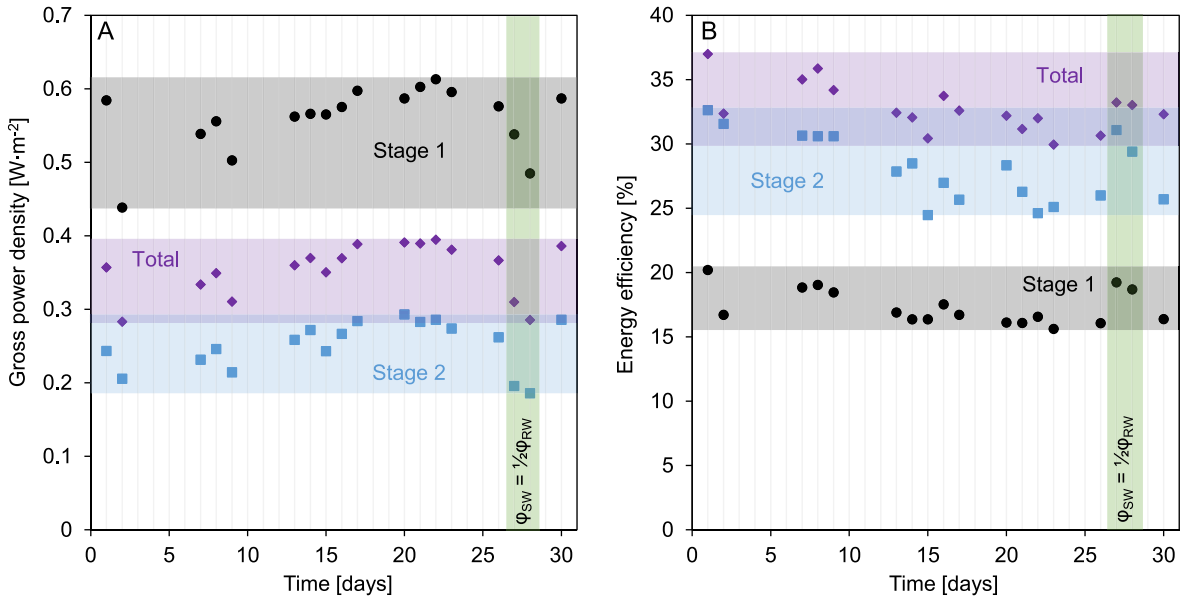

Fig. 3. Total and stage-related gross power density (A) and gross energy efficiency (B) for the sampling moments: Stage 1 (●), Stage 2 (■) and total (◆). The green shaded area corresponds to two days with an asymmetric flow rate, while RW was kept the same (39.3 L•h^{-1}), and SW was reduced to half (19.6 L•h^{-1}).

the salinity gradient of the natural waters was higher.

Some variations in performance as detected were explained by one of the following reasons: First, due to the natural change in salinity gradient between sea and river water (Figure S3A) and, second, due to changing the stack operation. For example, on days 27 and 28, an asymmetrical flow rate was tested (shaded green areas in Figs. 3, 4, 5 and 6), with the seawater flow rate being half of the river water flow rate, or change in current applied (Table S1). The temperature varied between 18 and 21 °C. These fluctuations can be seen in Figure S3.

Fig. 4 shows the multistage net power density (Eq. (S2)) and the pumping power density per stage in two scenarios (Eq. (S1)). If we would correct the gross power density only with the pressure drop of that stage to its starting value (0.30 bar for stage 1 and 0.15 bar for stage 2) and kept it constant, the total net power density amounts to 0.25 W•m^{-2}. However, due to an increasing pressure drop in stage 1, at the start of the operation (Figure S3), the total net power density was mostly below 0.10 W•m^{-2} (Fig. 4A). That is also why the constant and actual scenarios' net power density values do not match on day 1 of the 30-day run. Stage 1 was most affected, due to the higher flow velocity, and it was the first in line to experience a pressure drop increase due to fouling (Figure S3), reaching, for most days, pumping power densities higher than the gross power density (Fig. 4B). Later on, stage 2 also showed an increase in pressure drop, indicating the fouling was not exclusive to stage 1 but remained with positive net power density values. The net power density per stage can be obtained from the difference between Fig. 3A and Fig. 4B. In our previous work [30], it was shown that variation of the stack residence time (and hence flow velocity and pressure drop) could be used for the optimization of the net power

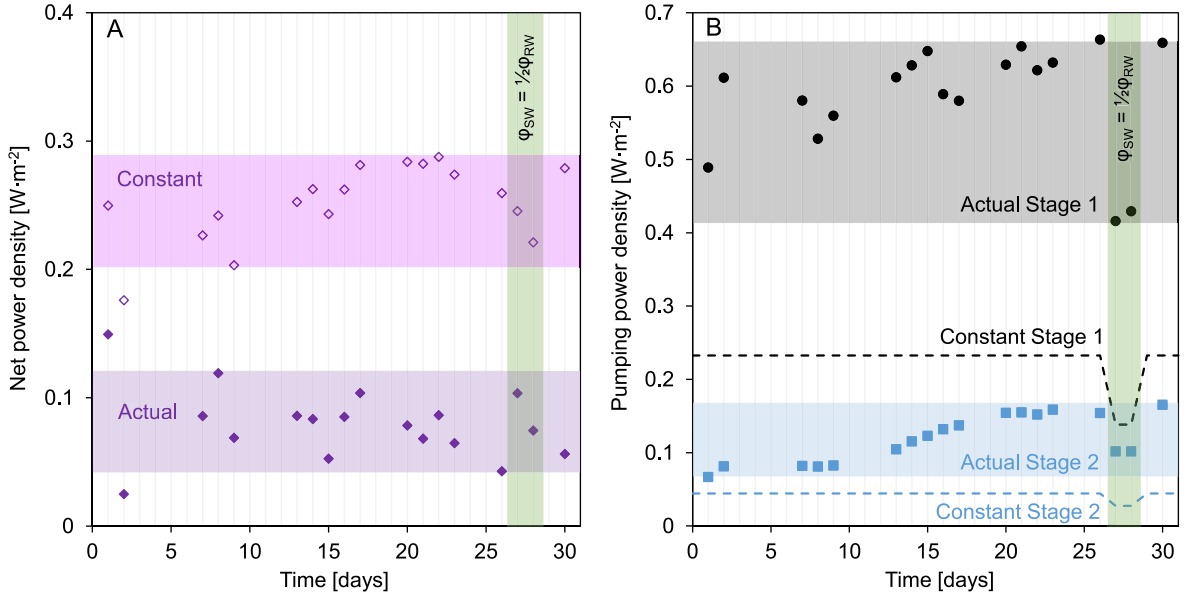

Fig. 4. (A) Total net power density of the multistage configuration for both the actual pressure drop and in case the pressure drop is taken as a constant and equal to the initial pressure drop. (B) Pumping power density calculated for stage 1 (black) and stage 2 (blue), actual values with symbols and constant values with dashed lines. The scenario actual uses the stage pressure drop at that moment and the scenario constant uses only the initial pressure drop value (Figure S5). The green shaded area corresponds to two days with an asymmetric flow rate, while RW was kept the same (39.3 L•h^{-1}), and SW was reduced to half (19.6 L•h^{-1}).

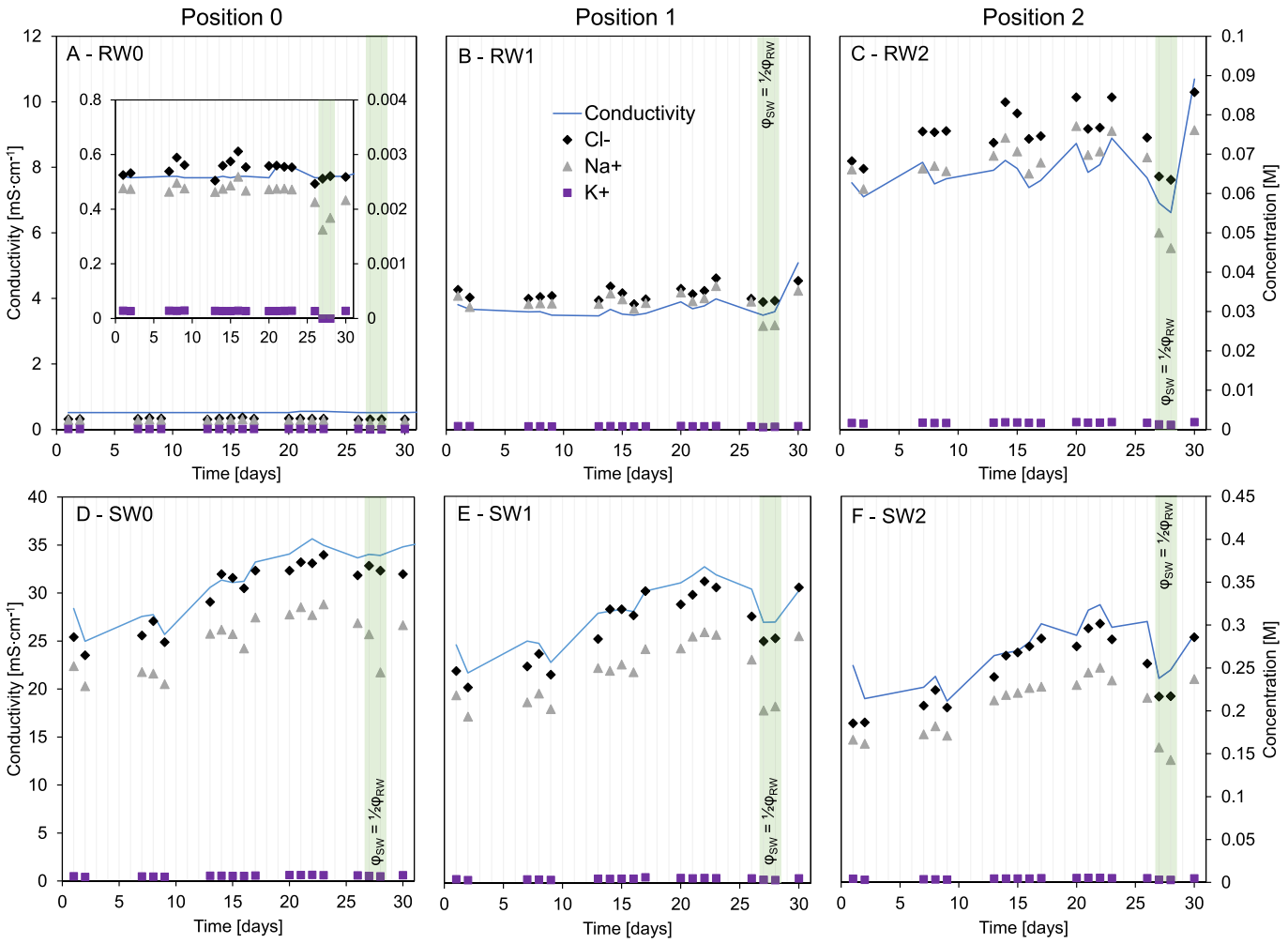

Fig. 5. Conductivity and concentration of monovalent ions at the inlet (position 0), between stages (position 1) and outlet (position 2) in river water (RW) (A, B and C) and in seawater (SW) (D, E and F) while operating at constant current density. The conductivity is represented with a line. The shaded area corresponds to two days with an asymmetric flow rate, RW was kept the same (39.3 L•h^{-1}), and SW was reduced to half (19.6 L•h^{-1}).

density production while increasing the energy efficiency. This strategy was not followed in this duration test.

The pressure drop can be partly attributed to visible fouling as algae growth was noticeable in the transparent tubing and the feedwater compartments. More details can be seen during the cleaning and stack autopsy in section 3.4. Interestingly, the gross electrical performance was not affected by the pressure increase and fouling [20]. We conclude that the electrical performance was dependent on the water's composition and concentration and mostly independent of the fouling for the period of testing. The fouling however affected the hydraulic performance, leading to a high loss in net power density output. Efforts towards maintaining the pumping power losses at a lower level in time are therefore needed.

The asymmetrical flow rate, with seawater being half of the river water flow rate, on days 27 and 28 did not show increasing performance values compared to the overall experiment. However, compared to the data points just before and after (days 26 and 30), which share more similar conditions, the energy efficiency increased (Fig. 3B). Although the gross power density decreased (Fig. 3A), the pumping power density lowered (Fig. 4B) subsequently increasing the net power density for the actual scenario. Thus, for controlled water conditions, the asymmetrical condition could work as an optimization. On the other hand, in a highly dynamic environment, as present in this study, there is no discernible benefit.

3.3. *Ions behaviour through staging: Multivalent ions are transported differently per stage*

During the 30-day run, natural waters were sampled at all positions to analyse the transport of ions through staging. The presence of multivalent ions, such as Mg^{2+}, Ca^{2+} and SO_4^{2-}, leads to uphill transport of these ions, as described by Vermaas et al. [10]. Uphill transport occurs when a divalent ion is transported against its concentration gradient (usually from the river water to the seawater side) to obtain equilibrium in chemical potential at both sides of the membrane. This phenomenon results in losses for the RED process, since one divalent ion like Mg^{2+} is exchanged with two monovalent ions like Na^+ at zero net charge.

Fig. 5 shows the concentration of monovalent ions through the multistage process and the measured conductivity at the inlet (position 0), between the stages (position 1) and at the outlet (position 2). Both for the river and seawater sides, the conductivity coincides with chloride (Cl^-) and sodium (Na^+) concentration, which means that conductivity sensors can correctly indicate the salinity gradient when the natural water is mainly composed of Cl^- and Na^+. This implies that an automated optimization of the RED performance could rely on the conductivity sensors that predict the available salinity gradient. All the monovalent ions show the same trend through staging.

While monovalent ions show a predictable behaviour through staging, multivalent ions have a different pattern. The uphill transport of sulphate (SO_4^{2-}) and calcium (Ca^{2+}) in stage 1 was expected and given in

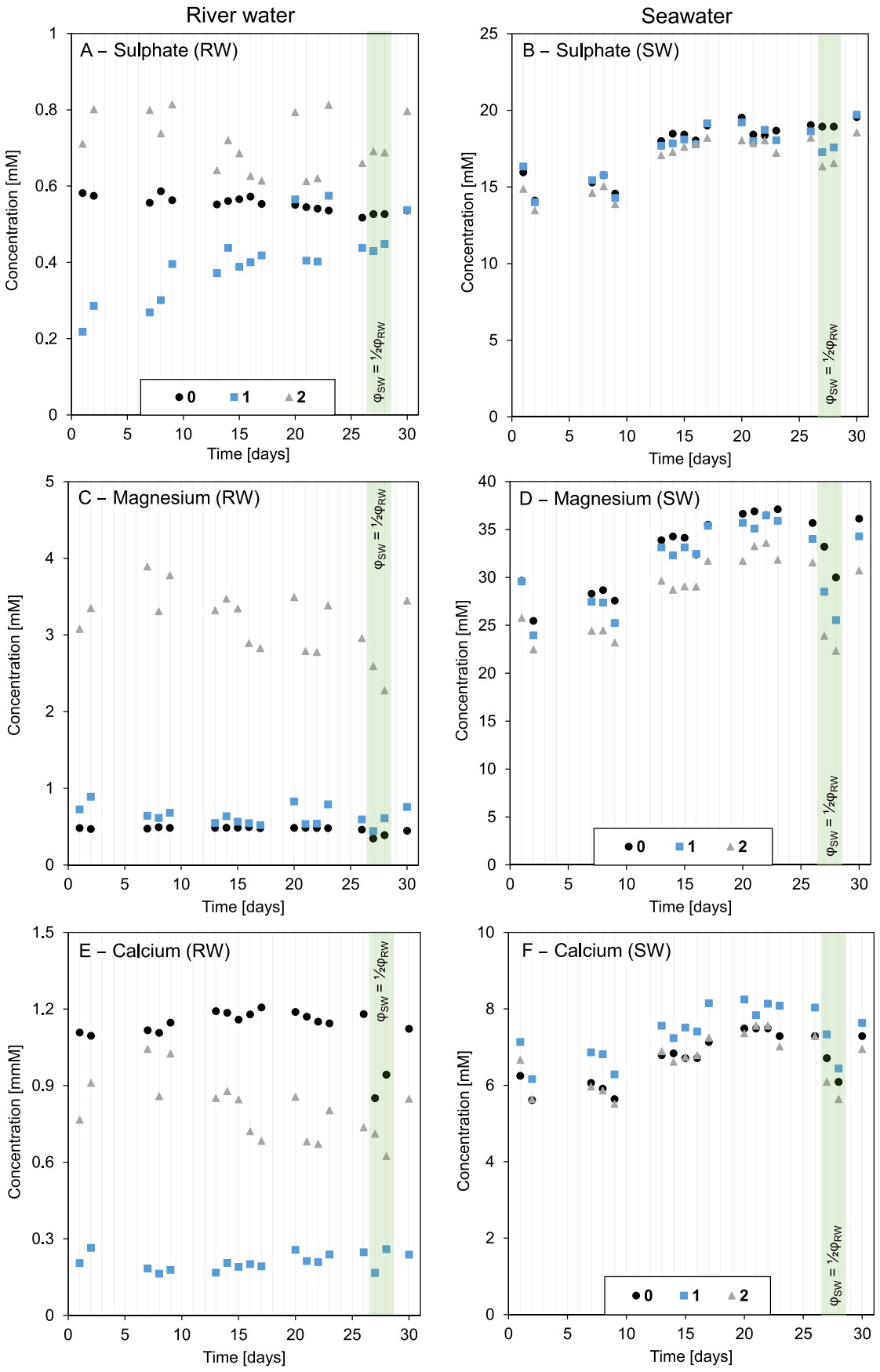

Fig. 6. Sulphate (A and B), magnesium (C and D) and calcium (E and F) concentrations, in mM, in river water (RW, left side graphs) and seawater (SW, right side graphs) at the inlet (position 0), between stages (position 1) and outlet (position 2). Note that the y-axis values differ between graphs. The green shaded area corresponds to two days with asymmetric flow rate, RW was kept the same (39.3 L•h^{-1}), and SW was reduced to half (19.6 L•h^{-1}).

the literature [14,51]. Fig. 6A and 6E show that both SO_4^{2-} and Ca^{2+} concentrations at the river water side decreased from position 0 to 1 (being 0 the inlet and 1 the outlet of stage 1). And the opposite occurred on the seawater side (Fig. 6B and 6F). In the case of magnesium (Mg^{2+}), uphill transport is not present (Fig. 6C and 6D) which is opposite to the literature [14]. In the work by Rijnaarts et al., the uphill transport of divalent ions was studied individually and not as a mixture, while also discarding the presence of Ca^{2+}. The uphill transport of Ca^{2+} can be explained by the smaller hydrated ionic radius of Ca $^{2+}$ (0.412 nm) compared to Mg^{2+} (0.428 nm) which makes Ca^{2+} being transported more easily than Mg^{2+}. Guo et al. [11] compared the uphill transport of Mg^{2+} and Ca^{2+} for two different membranes. At lower temperatures, most of the uphill transport was attributed to Ca^{2+} (which was ten times lower in concentration than Mg^{2+} at the river waterside). In our case, Ca^{2+} concentration (1.1 mM) in river water was higher than Mg^{2+} concentration (0.5 mM). The higher concentration and the smaller hydrated radii triggered Ca^{2+} to be preferably exchanged with Na^{+} rather than Mg^{2+}.

In stage 2, the transport pattern of multivalent ions was distinct from the previous stage. From positions 1 to 2, representing the inlet and outlet of stage 2, all ions follow downhill transport, following their concentration gradient, typically from the seawater to river water. Such behaviour has not been reported in the literature so far, given that experiments with multistage and multivalent ions are missing. The absence of uphill transport in stage 2 can be explained by the Donnan equilibrium. In stage 1, the multivalent ions exchange with the monovalent ions to obtain equilibrium in chemical potential between the membrane sides [52]. However, in stage 2, the Donnan potential for each ion is equilibrated at the inlet. Fig. 7 shows the calculated Donnan potential (Eq. (1)) for each ion on day 17 of the experiment. This day was randomly selected from the data. Stage 1 works as a removal step for multivalent ions, comparable to the principle of Donnan Dialysis [53]. The application of Donnan Dialysis as a pre-treatment step for RED was proposed earlier to improve the power density [54]. Since uphill transport was an intrinsic loss only for stage 1, stage 2 could benefit from this, resulting in a relatively better performance on that stage despite the lower salinity gradient.

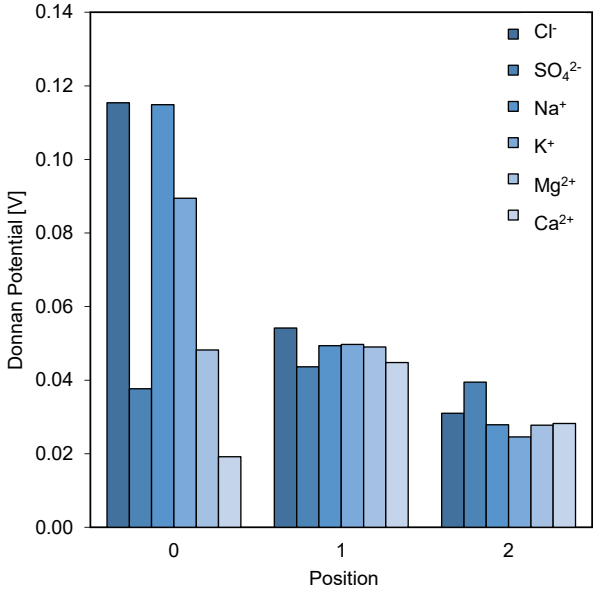

Fig. 7. Calculated Donnan Potentials (Eq. (1)) for the ions at the positions 0, 1 and 2 on day 17 (randomly selected to represent the data). Each bar represents an ion, from left to right: chloride, sulphate, sodium, potassium, magnesium and calcium.

3.4. Cleaning and stack autopsy

The anti-fouling strategies adopted in the pre-treatment were not able to maintain the stacks' pressure drop close to the initial values. Increasing pressure drops lead to higher pumping power losses which decrease the available net power density. Thus, towards the end of the experiment, in an attempt to lower the pressure drop and possibly recover the initial value, three physical cleaning techniques were selected regarding low cost, sustainability and short system interruption, and applied to both stacks. The cleaning started with reversing the inlet and outlet, followed by increased flow rate and finally air sparging. Results achieved with the application of these cleaning techniques are presented in Fig. 8.

The fouling removal on both stages was similar, achieving a recovery in pumping power losses of 0.03 W•m^{-2} for stage 1 and 0.01 W•m^{-2} for stage 2, which in both cases represented around 15 % of the pumping power that could be recovered from stage 1 (~0.21 W•m^{-2}) and stage 2 (~0.07 W•m^{-2}). A higher removal of fouling on stage 1 was expected since the flow velocity in this stage was higher and it was also more likely to accumulate foulants, as it was the first stack to receive the feed waters. Most likely that could not be detected due to the cleaning being performed only after a long time of operation when fouling build-up was already established and reached similar levels in both stages. When looking at the amount of particulate removed that could be collected in the outlet of the stacks we observed that on the seawater outlet of stage 1 a higher removal was achieved (Fig. 8). This indicates that more fouling was present and could be removed, even though the numbers presented are normalized for the membrane area, which in stage 2 is double of stage 1. For river water this did not happen, with similar removal in both stages, indicating that the fouling was not affected by the different hydraulic conditions of stages 1 and 2.

After the cleaning, two fractions of particulate fouling were analysed, the first one collected after the reverse and increased flow, and the second after air sparging. For the river water compartments of both stages, the particulate removal was greater with the reverse and increase

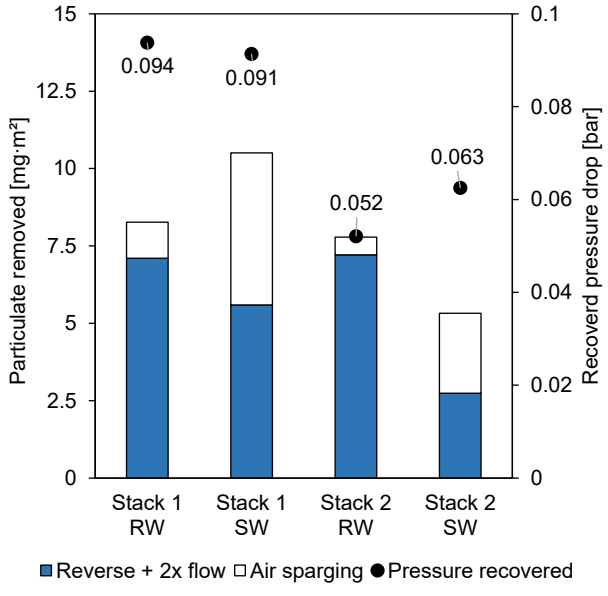

Fig. 8. Bars represent the amount of particulate fouling removed per stack membrane area for each step of the cleaning procedure: cleaning with reverse and increased flow together and air sparging. The pressure drop that could be recovered from each water compartment at the end of the cleaning is presented with a round symbol on top of the bars (difference between right before and after cleaning). The pressure drop decrease after the cleaning procedure appeared only to be a small fraction of the pressure drop across the stages after long term operation.

flow than with the air sparging. This probably happened due to the order in which the procedures took place, nonetheless, it showed that this simple technique could already remove a large part of the reversible fouling at a low energy cost and no additional agents had to be added (Fig. 8). For the seawater compartments of both stages, the removal of foulants with air sparging was similar to the amount achieved with the reverse and increased flow (around 50 % of total particulate removed), showing that the addition of compressed air as a cleaning agent could result in better cleaning. This indicates that the remaining fouling from seawater could still be removed with increased shear stress near the membrane surface as caused by the use of compressed air, tackling a more resistant fouling layer. This shows that a dedicated cleaning procedure has to be applied for a specific type of fouling.

The results show, that the pumping power recovered achieved with the cleaning procedure was quite modest (15 %) compared to the power losses accumulated on the previous days of operation. Implementing the cleaning method earlier in the operation and more frequent, may have prevented the cumulative increase of pressure drop [24]. In addition, other more intensive physical cleanings or chemical cleanings could be considered to reduce the fouling related pumping power losses [55].

Following the cleaning procedures, the configuration was kept running for two additional weeks to allow fouling regrowth and then stage 1 was opened for fouling investigation. Representative pictures of the membranes and spacers autopsy are shown in Figure S6. In the autopsy no particulate fouling was visible, nor types of fouling could be seen by the naked eye, except the presence of organic fouling by humic acids on the AEMs, due to the characteristically brown colour of this type of fouling [43]. The positive charge of the AEMs attracts the negatively charged organic matter commonly found in freshwater bodies, widely known as humic acids, while CEMs do not suffer from this specific type of fouling, due to their negative charge being able to repel such foulants. However, under the microscope, many types of foulant could be identified, as shown in Figs. 9 and 10.

Fig. 9A, 9B and 9C show agglomerations of organisms forming large structures, from 1 μm to approximately 50 μm. Most of the structures were identified as green algae, glaucophytes, and diatoms, all of them being commonly present in freshwater bodies [56,57]. The alcian blue dye reacted with biofilm and EPS layer, enabling their visualization and their presence was quite extensive on the surface of the membrane. SEM images, in Fig. 10A and 10B, show similar structures, and biofilm formation can be seen more clearly, with an agglomerate of bacterial cells surrounded by the EPS layer. These types of foulants are consistent with the pre-treatment that was employed during the experiment since with a 5 μm filter as the last step of pre-treatment, a large part of particulate fouling was retained and only smaller foulants could pass through. The formation of structures larger than 5 μm resulted from the growth of living organisms and aggregation in communities.

Fig. 9D and Fig. 10C and 10D also show an accumulation of fouling at the spacers at all four corners of the open mesh area. The presence of fouling reduced the available open area for the feedwaters to pass and consequently led to an increase in pressure drop. The spacers' thickness of 155 μm was remarkably thin and increased the sensitivity to fouling, which may also have contributed to an increase of the pressure on the inlet compartment [58].

Unfortunately, the cleaning procedures were not effective in removing the remaining pressure drop to a large extent, as the type of fouling in this experiment was more intrinsically connected to the membrane surface than loosely particulate deposits. For future studies, an anti-fouling strategy to be applied against biofouling growth could be avoiding sunlight to reach the stacks and tubing. In a darker setting,

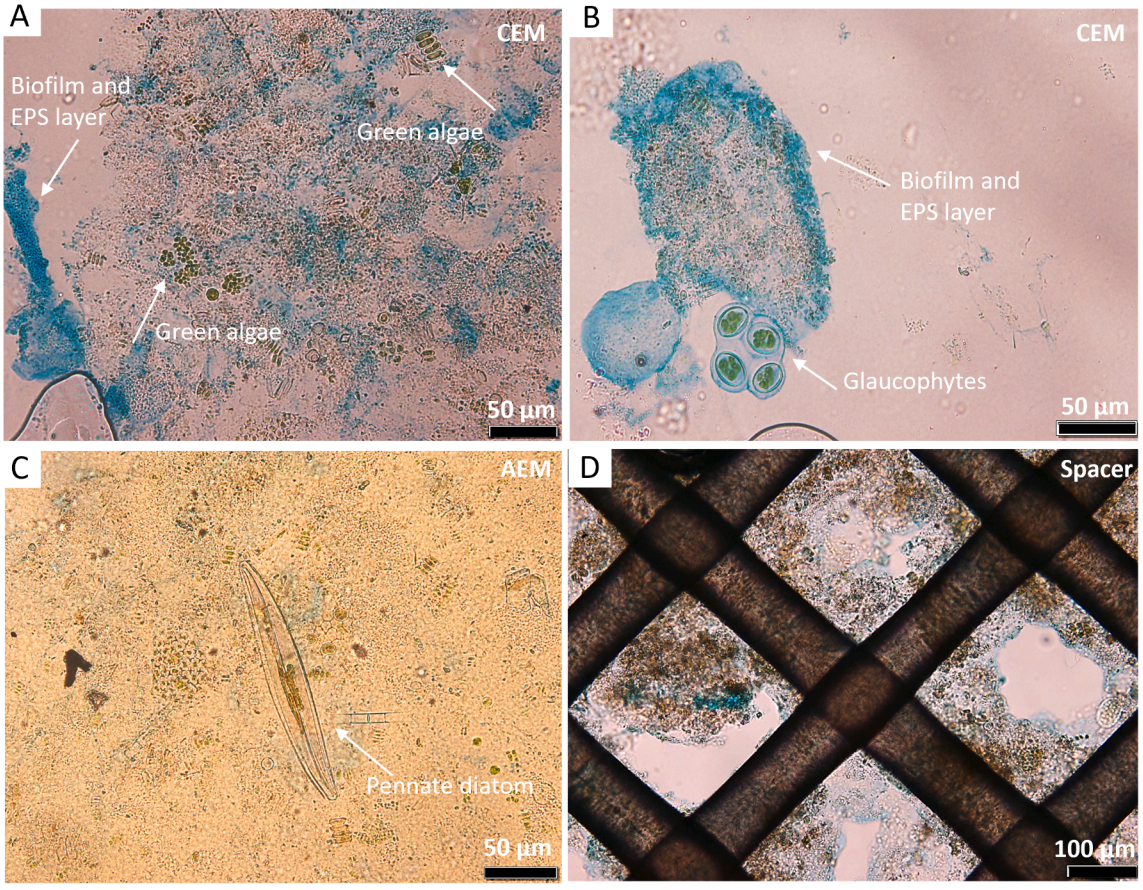

Fig. 9. Representative microscopic images of algae and other structures found on CEM (A and B), AEM (C) and spacer (D). The scale bar is 50 μm for A, B and C and 100 μm for D.

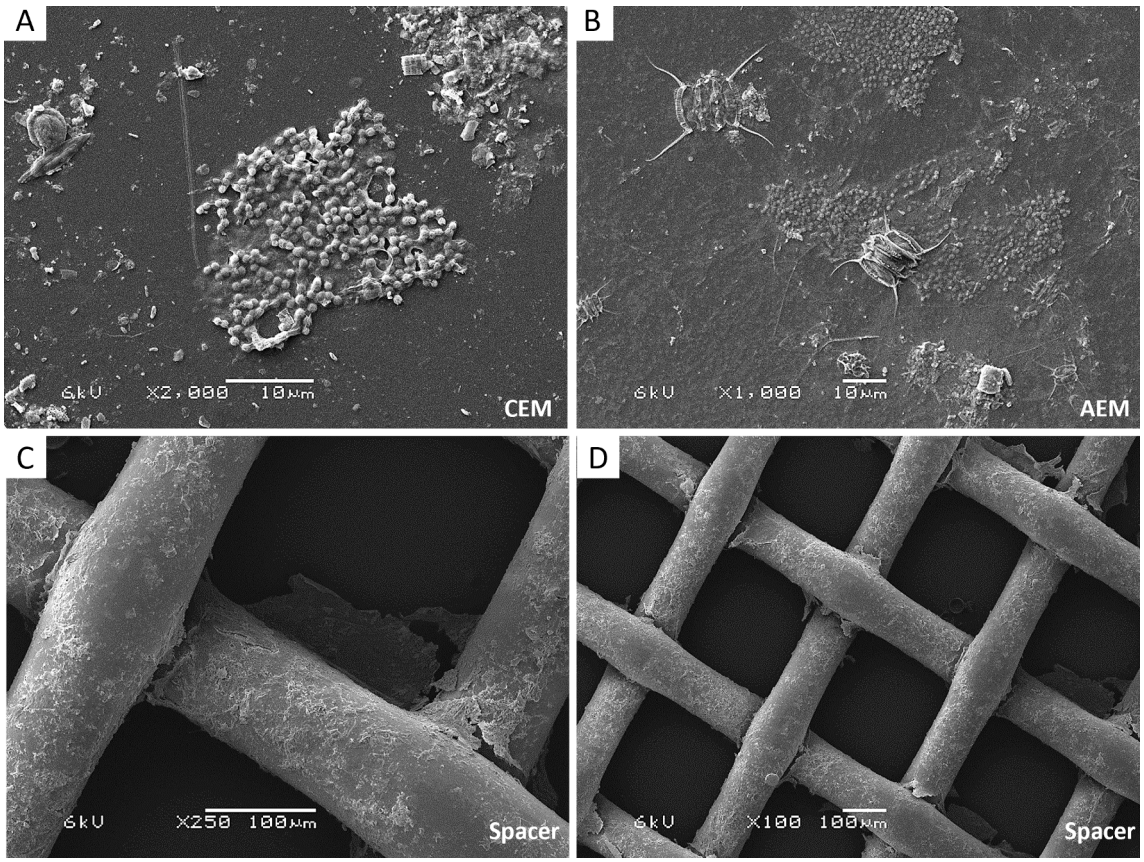

Fig. 10. Scanning electron microscope representative images of CEM (A), AEM (B) and spacers (C and D). The scale bar is 10 µm for A and B, and 100 µm for C and D.

most microorganisms' metabolism will be slower, preventing growth and accumulation [59]. Although there was a large effect of fouling on the hydraulic performance, the impact of fouling and scaling did not affect the gross electrical performance of the membrane pile, as the gross power density kept stable during the experiment. This positive outcome shows that the electrical optimization of the RED process (e.g. by multistage or electrode segmentation) and the minimization of the hydraulic resistance showed to be independent activities. The main influence of fouling was via the hydraulic resistance, affecting the required pumping power. This issue should be addressed using profiled membranes [25] or (in combination) with a more frequent cleaning procedure directly from the start of the experiment. The anti-fouling strategies (in pre-treatment and cleaning) should also be separately investigated and evaluated in view of their effectiveness, power consumption, system interruption and impact on environmental sustainability [20].

4. Conclusions

A multistage reverse electrodialysis system was operated with natural waters, at the Afsluitdijk, the Netherlands, for over 30 days with a stable gross electrical performance. The gross power density was between 0.3 and 0.4 W•m^{-2} and energy efficiency values were between 30 and 37 %. A strong increase in pressure drop in stage 1 was observed in the first weeks, after which the net power density was stable at around 0.1 W•m^{-2}. Considering the initial measured pressure drop the net power density would increase to around 0.25 W•m^{-2}. Fouling did not affect the gross electrical performance of both stages but led to a higher pressure drop reducing the net power density output. The transport of multivalent ions was different in stage 1 and stage 2. For stage 1, SO_4^{2-} and Ca^{2+} showed uphill transport from river water to seawater, whereas Mg^{2+}, which is often linked to uphill transport in literature, did not. This was explained by the higher concentration of Ca^{2+} than Mg^{2+} in the river water. In stage 2 actually, no uphill transport was observed. The cleaning procedures applied had limited effect on recovering the original pressure drop of the stacks. Stack autopsy revealed, at the membrane surface, microorganism structures larger than the cartridge filter (mean pore size of 5 µm) used as pre-treatment for the natural waters. The agglomeration and growth of these structures in-situ contributed to the increase in pressure drop through time in the compartments, as well as part of the spacers' open area that was covered with (bio)fouling.

Multistage reverse electrodialysis, with two stages in series, showed as a viable configuration to increase the energy efficiency with a stable gross power density, even at the low salinity gradient, available in this duration test. For optimal performance, the electrical control of the stages could be automated, taking into consideration the conductivity at the inlets and actual pressure drop. An improved stack design in combination with pre-treatment of the natural waters and periodical cleaning procedure of the stages is highly recommended, to avoid the power losses associated with the pressure drop increase across the stacks.

CRediT authorship contribution statement

Catarina Simões: Conceptualization, Methodology, Investigation, Visualization, Writing – original draft. **Bárbara Vital:** Methodology, Investigation, Writing – original draft. **Tom Sleutels:** Supervision, Writing – review & editing. **Michel Saakes:** Conceptualization, Supervision, Writing – review & editing, Project administration. **Wim Brilman:** Conceptualization, Supervision, Writing – review & editing.

Declaration of Competing Interest

The authors declare that they have no known competing financial

interests or personal relationships that could have appeared to influence the work reported in this paper.

Data availability

Data will be made available on request.

Acknowledgements

This work was performed in the cooperation framework of Wetsus, European Centre of Excellence for Sustainable Water Technology (www.wetsus.eu). Wetsus is co-funded by the Dutch Ministry of Economic Affairs and Ministry of Infrastructure and Environment, the Province of Fryslân, and the Northern Netherlands Provinces. This project has also received funding from the European Union's Horizon 2020 research and innovation program under the Marie Skłodowska-Curie grant agreement No 665874. The authors would like to thank the participants of the research theme "Blue Energy" for their input and suggestions and their financial support.

Appendix A. Supplementary data

Supplementary data to this article can be found online at https://doi.org/10.1016/j.cej.2022.138412.

References

[1] K. Nijmeijer, S. Metz, Chapter 5 Salinity Gradient Energy, Elsevier, 2010. https://doi.org/10.1016/S1871-2711(09)00205-0.
[2] R.E. Lacey, Energy by reverse electrodialysis, Ocean Eng. 7 (1980) 1–47, https://doi.org/10.1016/0029-8018(80)90030-x.
[3] J. Veerman, M. Saakes, S.J. Metz, G.J. Harmsen, Reverse electrodialysis: Evaluation of suitable electrode systems, J. Appl. Electrochem. 40 (8) (2010) 1461–1474.
[4] R.E. Pattle Production of electric power by mixing fresh and salt water in the hydroelectric pile Nature. 174 4431 1954 660 660.
[5] A. Nazif, H. Karkhanechi, E. Saljoughi, S.M. Mousavi, H. Matsuyama, Recent progress in membrane development, affecting parameters, and applications of reverse electrodialysis: A review, J. Water Process Eng. 47 (2022), 102706, https://doi.org/10.1016/j.jwpe.2022.102706.
[6] Y. Mei, C.Y. Tang, Recent developments and future perspectives of reverse electrodialysis technology: A review, Desalination 425 (2018) 156–174.
[7] R.A. Tufa, S. Pawlowski, J. Veerman, K. Bouzek, E. Fontananova, G. di Profio, S. Velizarov, J. Goulão Crespo, K. Nijmeijer, E. Curcio, Progress and prospects in reverse electrodialysis for salinity gradient energy conversion and storage, Appl. Energy 225 (2018) 290–331, https://doi.org/10.1016/j.apenergy.2018.04.111.
[8] J.W. Post, C.H. Goeting, J. Valk, S. Goinga, J. Veerman, H.V.M. Hamelers, P.J.F. M. Hack, Towards implementation of reverse electrodialysis for power generation from salinity gradients, Desalin. Water Treat. 16 (2010) 182–193, https://doi.org/10.5004/dwt.2010.1093.
[9] J.W. Post, H.V.M. Hamelers, C.J.N. Buisman, Influence of multivalent ions on power production from mixing salt and fresh water with a reverse electrodialysis system, J. Membr. Sci. 330 (1-2) (2009) 65–72.
[10] D.A. Vermaas, J. Veerman, M. Saakes, K. Nijmeijer, Influence of multivalent ions on renewable energy generation in reverse electrodialysis, Energy Environ. Sci. 7 (4) (2014) 1434–1445.
[11] Z.Y. Guo, Z.Y. Ji, Y.G. Zhang, F.J. Yang, J. Liu, Y.Y. Zhao, J.S. Yuan, Effect of ions (K+, Mg2+, Ca2+ and SO42−) and temperature on energy generation performance of reverse electrodialysis stack, Electrochim. Acta 290 (2018) 282–290, https://doi.org/10.1016/j.electacta.2018.09.015.
[12] A.H. Avci, R.A. Tufa, E. Fontananova, G. di Profio, E. Curcio, Reverse Electrodialysis for energy production from natural river water and seawater, Energy. 165 (2018) 512–521, https://doi.org/10.1016/j.energy.2018.09.111.
[13] E. Güler, W. van Baak, M. Saakes, K. Nijmeijer, Monovalent-ion-selective membranes for reverse electrodialysis, J. Membr. Sci. 455 (2014) 254–270.
[14] T. Rijnaarts, E. Huerta, W. van Baak, K. Nijmeijer, Effect of divalent cations on RED performance and cation exchange membrane selection to enhance power densities, Environ. Sci. Technol. 51 (21) (2017) 13028–13035.
[15] S. Mehdizadeh, Y. Kakihana, T. Abo, Q. Yuan, M. Higa, Power generation performance of a pilot-scale reverse electrodialysis using monovalent selective ion-exchange membranes, Membranes (Basel). 11 (2021) 1–25, https://doi.org/10.3390/membranes11010027.
[16] E.H. Hossen, Z.E. Gobetz, R.S. Kingsbury, F. Liu, H.C. Palko, L.L. Dubbs, O. Coronell, D.F. Call, Temporal variation of power production via reverse electrodialysis using coastal North Carolina waters and its correlation to temperature and conductivity, Desalination 491 (2020), 114562, https://doi.org/10.1016/j.desal.2020.114562.
[17] S. Mehdizadeh, M. Yasukawa, T. Abo, M. Kuno, Y. Noguchi, M. Higa, The effect of feed solution temperature on the power output performance of a pilot-scale reverse electrodialysis (RED) system with different intermediate distance, Membranes (Basel). 9 (6) (2019) 73.
[18] D.A. Vermaas, D. Kunteng, M. Saakes, K. Nijmeijer, Fouling in reverse electrodialysis under natural conditions, Water Res. 47 (3) (2013) 1289–1298.
[19] R.S. Kingsbury, F. Liu, S. Zhu, C. Boggs, M.D. Armstrong, D.F. Call, O. Coronell, Impact of natural organic matter and inorganic solutes on energy recovery from five real salinity gradients using reverse electrodialysis, J. Membr. Sci. 541 (2017) 621–632, https://doi.org/10.1016/j.memsci.2017.07.038.
[20] B. Vital, E.V. Torres, T. Sleutels, M.C. Gagliano, M. Saakes, H.V.M. Hamelers, Fouling fractionation in reverse electrodialysis with natural feed waters demonstrates dual media rapid filtration as an effective pre-treatment for fresh water, Desalination 518 (2021) 115277.
[21] D.A. Vermaas, D. Kunteng, J. Veerman, M. Saakes, K. Nijmeijer, Periodic feedwater reversal and air sparging as antifouling strategies in reverse electrodialysis, Environ. Sci. Technol. 48 (5) (2014) 3065–3073.
[22] J. Moreno, N. de Hart, M. Saakes, K. Nijmeijer, CO 2 saturated water as two-phase flow for fouling control in reverse electrodialysis, Water Res. 125 (2017) 23–31.
[23] E.J. Bodner, M. Saakes, T. Sleutels, C.J.N. Buisman, H.V.M. Hamelers, The RED Fouling Monitor: A novel tool for fouling analysis, J. Membr. Sci. 570-571 (2019) 294–302.
[24] D. Pintossi, M. Saakes, Z. Borneman, K. Nijmeijer, Electrochemical impedance spectroscopy of a reverse electrodialysis stack: A new approach to monitoring fouling and cleaning, J. Power Sources 444 (2019), 227302, https://doi.org/10.1016/j.jpowsour.2019.227302.
[25] D.A. Vermaas, M. Saakes, K. Nijmeijer, Power generation using profiled membranes in reverse electrodialysis, J. Membr. Sci. 385-386 (2011) 234–242.
[26] S. Pawlowski, T. Rijnaarts, M. Saakes, K. Nijmeijer, J.G. Crespo, S. Velizarov, Improved fluid mixing and power density in reverse electrodialysis stacks with chevron-profiled membranes, J. Membr. Sci. 531 (2017) 111–121.
[27] J.Y. Nam, K.S. Hwang, H.C. Kim, H. Jeong, H. Kim, E. Jwa, S.C. Yang, J. Choi, C. S. Kim, J.H. Han, N. Jeong, Assessing the behavior of the feed-water constituents of a pilot-scale 1000-cell-pair reverse electrodialysis with seawater and municipal wastewater effluent, Water Res. 148 (2019) 261–271, https://doi.org/10.1016/j.watres.2018.10.054.
[28] C. Simões, D. Pintossi, M. Saakes, Z. Borneman, W. Brilman, K. Nijmeijer, Electrode segmentation in reverse electrodialysis: Improved power and energy efficiency, Desalination 492 (2020) 114604.
[29] J. Hu, S. Xu, X.i. Wu, D. Wu, D. Jin, P. wang, Q. Leng, Multi-stage reverse electrodialysis: Strategies to harvest salinity gradient energy, Energy Convers. Manage. 183 (2019) 803–815.
[30] C. Simões, D. Pintossi, M. Saakes, W. Brilman, Optimizing multistage reverse electrodialysis for enhanced energy recovery from river water and seawater: Experimental and modeling investigation, Adv. Appl. Energy. 2 (2021) 100023.
[31] J. Veerman, M. Saakes, S.J. Metz, G.J. Harmsen, Reverse electrodialysis: Performance of a stack with 50 cells on the mixing of sea and river water, J. Membr. Sci. 327 (1-2) (2009) 136–144.
[32] J. Veerman, Reverse electrodialysis : Co- and counterflow optimization of multistage configurations for maximum energy efficiency, Membranes (Basel) (2020) 1–13, https://doi.org/10.3390/membranes10090206.
[33] M. Tedesco, P. Mazzola, A. Tamburini, G. Micale, I.D.L. Bogle, M. Papapetrou, A. Cipollina, Analysis and simulation of scale-up potentials in reverse electrodialysis, Desalin. Water Treat. 55 (12) (2015) 3391–3403.
[34] J. Hu, S. Xu, X.i. Wu, S. Wang, X. Zhang, S. Yang, R. Xi, D. Wu, L. Xu, Experimental investigation on the performance of series control multi-stage reverse electrodialysis, Energy Convers. Manage. 204 (2020) 112284.
[35] Z. Wang, J. Li, C. Zhang, H. Wang, X. Kong, Power production from seawater and discharge brine of thermal desalination units by reverse electrodialysis, Appl. Energy 314 (2022) 118977.
[36] S. Xu, Q. Leng, X.I. Wu, Z. Xu, J. Hu, D. Wu, D. Jing, P. Wang, F. Dong, Influence of output current on decolorization efficiency of azo dye wastewater by a series system with multi-stage reverse electrodialysis reactors, Energy Convers. Manage. 228 (2021) 113639.
[37] J. Hu, S. Xu, X. Wu, D. Wu, D. Jin, P. Wang, Q. Leng, Theoretical simulation and evaluation for the performance of the hybrid multi-effect distillation—reverse electrodialysis power generation system, Desalination 443 (2018) 172–183, https://doi.org/10.1016/j.desal.2018.06.001.
[38] Y. Zhang, X.I. Wu, S. Xu, Q. Leng, S. Wang, A serial system of multi-stage reverse electrodialysis stacks for hydrogen production, Energy Convers. Manage. 251 (2022) 114932.
[39] D. Pintossi, C. Simões, M. Saakes, Z. Borneman, K. Nijmeijer, Predicting reverse electrodialysis performance in the presence of divalent ions for renewable energy generation, Energy Convers. Manage. 243 (2021) 114369.
[40] J. Moreno, E. Slouwerhof, D.A. Vermaas, M. Saakes, K. Nijmeijer, The breathing cell: Cyclic intermembrane distance variation in reverse electrodialysis, Environ. Sci. Technol. 50 (20) (2016) 11386–11393.
[41] P. Dlugolecki, K. Nymeijer, S. Metz, M. Wessling, Current status of ion exchange membranes for power generation from salinity gradients, J. Membr. Sci. 319 (1-2) (2008) 214–222.
[42] J. Moreno, S. Grasman, R. van Engelen, K. Nijmeijer, Up-scaling reverse electrodialysis, Environ. Sci. Technol. 52 (18) (2018) 10856–10863.
[43] T. Rijnaarts, J. Moreno, M. Saakes, W.M. de Vos, K. Nijmeijer, Role of anion exchange membrane fouling in reverse electrodialysis using natural feed waters, Colloids Surf., A 560 (2019) 198–204, https://doi.org/10.1016/j.colsurfa.2018.10.020.

[44] X. Ge, X. Wang, M. Zhang, S. Seetharaman, Correlation and prediction of activity and osmotic coefficients of aqueous electrolytes at 298.15 K by the modified TCPC model, J. Chem. Eng. Data 52 (2) (2007) 538–547.
[45] D.A. Vermaas, J. Veerman, N.Y. Yip, M. Elimelech, M. Saakes, K. Nijmeijer, High efficiency in energy generation from salinity gradients with reverse electrodialysis, ACS Sustainable Chem. Eng. 1 (10) (2013) 1295–1302.
[46] L.S. Clesceri, A.E. Greenberg, A, 22th Edition, D. Eaton, Standard Methods for the Examination of Water and Wastewater, 1999.
[47] A.W. Qurashi, A.N. Sabri, Biofilm formation in moderately halophilic bacteria is influenced by varying salinity levels, J. Basic Microbiol. 52 (2012) 566–572, https://doi.org/10.1002/jobm.201100253.
[48] J. Veerman, J.W. Post, M. Saakes, S.J. Metz, G.J. Harmsen, Reducing power losses caused by ionic shortcut currents in reverse electrodialysis stacks by a validated model, J. Membr. Sci. 310 (1-2) (2008) 418–430.
[49] A. Culcasi, L. Gurreri, A. Zaffora, A. Cosenza, A. Tamburini, A. Cipollina, G. Micale, Ionic shortcut currents via manifolds in reverse electrodialysis stacks, Desalination 485 (2020) 114450.
[50] N.Y. Yip, D.A. Vermaas, K. Nijmeijer, M. Elimelech, Thermodynamic, energy efficiency, and power density analysis of reverse electrodialysis power generation with natural salinity gradients, Environ. Sci. Technol. 48 (2014) 4925–4936, https://doi.org/10.1021/es5005413.
[51] D. Pintossi, C.L. Chen, M. Saakes, K. Nijmeijer, Z. Borneman, Influence of sulfate on anion exchange membranes in reverse electrodialysis, npj Clean Water 3 (2020) 1–10, https://doi.org/10.1038/s41545-020-0073-7.
[52] M. Higa, A. Tanioka, K. Miyasaka, Simulation of the transport of ions against their concentration gradient across charged membranes, J. Membr. Sci. 37 (1988) 251–266, https://doi.org/10.1016/S0376-7388(00)82432-1.
[53] M. Vanoppen, G. Stoffels, C. Demuytere, W. Bleyaert, A.R.D. Verliefde, Increasing RO efficiency by chemical-free ion-exchange and Donnan dialysis: Principles and practical implications, Water Res. 80 (2015) 59–70, https://doi.org/10.1016/j.watres.2015.04.030.
[54] T. Rijnaarts, N.T. Shenkute, J.A. Wood, W.M. de Vos, K. Nijmeijer, Divalent cation removal by donnan dialysis for improved reverse electrodialysis, ACS Sustainable Chem. Eng. 6 (5) (2018) 7035–7041.
[55] K. Chon, N. Jeong, H. Rho, J.Y. Nam, E. Jwa, J. Cho, Fouling characteristics of dissolved organic matter in fresh water and seawater compartments of reverse electrodialysis under natural water conditions, Desalination 496 (2020), 114478, https://doi.org/10.1016/j.desal.2020.114478.
[56] L.O. Villacorte, S.A.A. Tabatabai, N. Dhakal, G. Amy, J.C. Schippers, M. D. Kennedy, Algal blooms: an emerging threat to seawater reverse osmosis desalination, Desalin. Water Treat. 55 (2015) 2601–2611, https://doi.org/10.1080/19443994.2014.940649.
[57] T.H. Tan, C.P. Leaw, S. Chee, Y. Leong, L.P. Lim, S.M. Chew, Marine microphytoplankton of Singapore, with a review of harmful microalgae in the region, Raffles Bulletin of Zoology (2016).
[58] J. Choi, W.-S. Kim, H.K. Kim, S.C. Yang, J.-H. Han, Y.C. Jeung, N.J. Jeong, Fouling behavior of wavy-patterned pore-filling membranes in reverse electrodialysis under natural seawater and sewage effluents, npj Clean Water 5 (2022) 1–12, https://doi.org/10.1038/s41545-022-00149-2.
[59] J. Landoulsi, K.E. Cooksey, V. Dupres, Review - Interactions between diatoms and stainless steel: Focus on biofouling and biocorrosion, Biofouling. 27 (2011) 1105–1124, https://doi.org/10.1080/08927014.2011.629043.